Micro X-Ray computed tomography imaging and ultrasonic velocity measurements in tetrahydrofuran-hydrate-bearing sediments

Mandy Schindler*, Michael L. Batzle[†] and Manika Prasad

Colorado School of Mines, 1500 Illinois Street, Golden, CO 80401, USA

ABSTRACT

Naturally occurring gas hydrates contain significant amounts of natural gas that might be produced as an energy resource in the foreseeable future. Thus, it is necessary to understand the pore-space characteristics of hydrate reservoirs, particularly the pore-scale distribution of the hydrate and its interaction with the sediment. Four end-member models for hydrate distribution in the pore space are pore filling, sediment-frame component, envelope cementing, and contact cementing. The goal of this study is to compare the models with pore-scale hydrate distributions obtained in laboratory-formed hydrates. Our results verify hydrate pore-scale distributions by direct, visual observations that were previously implied by indirect, elastic property measurements.

Laboratory measurements were conducted using tetrahydrofuran as a guest molecule since tetrahydrofuran hydrate can be used as a proxy for naturally occurring hydrates. We performed micro X-ray computed tomography to obtain information about the distribution of hydrate in the pore space of synthetic sediment (glass beads). We also made ultrasonic velocity measurements on the same samples. Micro X-ray computed tomography images and ultrasonic velocity measurements both indicate that the tetrahydrofuran hydrate forms in the pore space with a part of the hydrate bridging the grains without touching the grain surfaces. These hydrate-bearing sediments appear to follow a pore-filling model with a portion of the hydrate becoming a load-bearing part of the sediment frame.

Key words: Gas hydrate, Rock physics, Ultrasonic velocities.

INTRODUCTION

Gas hydrates are clathrate structures of natural gases. They require low temperatures and high pressures for stability. The widespread occurrence of gas hydrates in permafrost and shallow marine sediments along continental slopes is well established (Collett *et al.* 2009). The estimated amount of natural gas, mainly methane, stored in hydrate reservoirs exceeds the amount of natural gas stored in conventional resources by at least one order of magnitude (Meyer 1981; Dobrynin, Korotajev, and Plyuschev; Collett *et al.* 2009). Anderson *et al.* (2008) and Dallimore *et al.* (2008)

demonstrated that gas-hydrate production can be developed with existing oil and gas production technology, but before successfully producing methane gas from hydrate reservoirs, we need to attain knowledge about physical properties of gas-hydrate-bearing sediments.

The most common geophysical methods used to characterise and quantify gas hydrates in nature are seismic surveying and well logging. To calibrate and interpret these field measurements, laboratory studies are necessary to determine the bulk physical properties of hydrate-bearing sediments. Hydrate saturations are commonly derived from electrical resistivity logs; however, to avoid the use of empirical relationships between resistivity logs and seismic data, we want to base our estimation of hydrate saturation on velocities and use models

---

*E-mail: manschin@mines.edu
[†]deceased
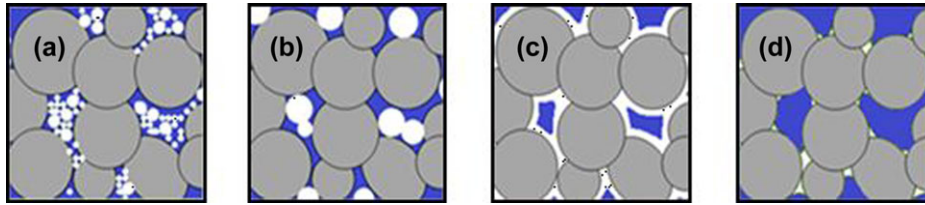
Figure 1 Conceptual images of possible hydrate distributions in the pore space. Grey spheres represent sediment grains, pore fluid (e.g., brine) is shown in blue, and the hydrate is shown in white. (a) Pore-filling hydrate. (b) Frame-component hydrate. (c) Envelope-cementing hydrate. (d) Contact-cementing hydrate. Figures modified from Rydzy and Batzle (2011).

that work for acoustic logs and seismic surveys. Currently, it is possible to predict the existence of gas hydrates from geophysical measurements. However, the techniques used to estimate hydrate saturation based on either seismic data or acoustic logs require further development (Collett and Lee 2012). The amount of gas hydrates stored in a reservoir remains uncertain because the relationship between saturation and seismic or sonic velocities depends largely on the pore-scale distribution of gas hydrates. Gas hydrates occur as massive units and lenses in fractures of fine-grained material (shale) as well as distributed in the pore space of coarse-grained porous media (Fig. 1). The models described by Ecker, Dvorkin, and Nur (1998) and Helgerud *et al.* (1999) show that a very small amount of cementing gas hydrates presents itself with similar velocities as a high saturation of pore-filling gas hydrates. Thus, information about the distribution of gas hydrates in a rock is necessary to determine hydrate saturation. It is imperative to ascertain hydrate–sediment interactions in addition to physical properties of pure hydrates (Yun *et al.* 2005).

In this study, we focus on the pore-scale distribution of gas hydrates in synthetic coarse-grained porous media with high permeability. Coarse-grained sand reservoirs, as they exist in permafrost regions and marine environments, have high permeability and high hydrate saturations, allowing effective production and relatively easy access, and are thus more likely to permit methane production from gas hydrates than hydrate reservoirs in shale (Boswell and Collett 2006).

Hydrate distribution in the pore space depends mainly on the formation method. In nature, gas hydrates are formed in two ways: (i) from methane dissolved in water or (ii) from free methane gas (Collett *et al.* 2009). Hydrates formed from methane gas tend to form at the grain surface and grain contacts (Waite, Winters, and Mason 2004; Priest, Best, and Clayton 2005), whereas hydrates formed from methane dissolved in water tend to form in the pore body with little or no contact to the sediment grains (Ecker *et al.* 1998; Kunerth *et al.* 2001). These conclusions are based on the velocities matching

the models; however, to date, there is little direct verification for the pore-scale distribution. Very limited research has been done on imaging hydrate distribution in the pore space (e.g., Sothcott *et al.* (2007), Kerkar *et al.* (2009, 2014), and Chaouachi *et al.* (2015)). Our study provides imaging of the pore-space distribution of hydrates as well as ultrasonic P-wave and S-wave velocities, thus providing a link between the effective medium models and direct visual observations of hydrates in the pore space.

Gas hydrates in coarse-grained, marine sediments are more likely to form from methane dissolved in water, whereas gas hydrates in permafrost regions are associated with formation from free methane gas (Collett *et al.* 2009). Our goal is to determine the pore-scale distribution of hydrates formed from gas dissolved in water and the corresponding ultrasonic velocities. As a proxy for this formation mechanism, we use tetrahydrofuran as a guest molecule. We use micro X-ray computed tomography to image hydrate distribution in the pore space. In addition, we investigate the influence of hydrate saturation and distribution on ultrasonic velocities. The relation between pore-scale distribution, the hydrate formation method, and velocities is essential to determine the amount of hydrates in a reservoir from seismic data and sonic logs.

Effective medium modeling

Seismic and acoustic velocities are influenced by changes in hydrate saturation. However, in addition to hydrate saturation, velocities will behave differently for different hydrate distributions in the pore space. Theoretical models infer different pore-scale hydrate distributions and their impact on acoustic velocities. One such model is the effective medium theory developed by Dvorkin, Nur, and Yin (1994) and Dvorkin and Nur (1996) and applied to hydrate-bearing sediments by Ecker *et al.* (1998) and Helgerud *et al.* (1999).

Figure 1 shows four different pore-scale distributions according to this effective medium model for gas hydrates in

sediment: contact cementing, envelope cementing, pore filling, and load bearing. The contact-cementing hydrate causes a drastic increase in ultrasonic velocities even for small amounts of the hydrate present in the pore space since the hydrate becomes part of the dry sediment frame and bonds the sediment grains together, leading to an increase the frame stiffness. The hydrate formed according to the pore-filling model shows a much smaller influence on the ultrasonic velocities as the hydrate is considered part of the pore fluid and does thus only change the elastic properties of the fluid without having an influence on the stiffness of the dry sediment frame. Hydrate formation from free gas appears to create a grain-cementing hydrate, which resembles the contact or envelope-cementing models (Waite *et al.* 2004; Priest *et al.* 2005; Chand *et al.* 2006). The hydrate formation for this method starts at the interface of free gas and water and grows into the water phase. A cementing hydrate mimics the initial water saturation of the samples (Waite *et al.* 2004; Ebinuma *et al.* 2005). A hydrate formed from gas dissolved in water seems to have little or no contact with the sediment grains and thus conforms to the frame-component or pore-filling model (Kerkar *et al.* 2014). For this method, the hydrate nucleation starts at the grain surfaces, and the hydrate grows into the pore space (Waite *et al.* 2009). Laboratory measurements are necessary to determine the correlation of hydrate distribution in the pore space with ultrasonic velocities and to corroborate previous results.

MATERIALS AND METHOD

We utilised micro X-ray computed tomography (CT) and ultrasonic velocity measurements. Micro CT was used for direct visual observation of the pore-space hydrate distribution. Ultrasonic velocity measurements were used to show how the velocities change for different hydrate saturations. The combination of these two measurements can be compared with effective medium models. The materials in the sample were borosilicate glass beads as host sediment, tetrahydrofuran (THF) as the guest molecule and methane proxy, and deionised water mixed with barium chloride to obtain a density contrast between the THF hydrate and residual brine.

Proxy for natural gas hydrates

The most common hydrate in nature is methane (CH_4) hydrate. Methane hydrates either need to be cooled to $-78.7\,°C$ to be stable under atmospheric pressure (Sloan and Koh 2008)

or require a pressure of 4 MPa to be stable at 4 °C (Carroll, 2009). The controlled synthesis of methane hydrates from the aqueous phase is additionally difficult because of the low solubility of methane in water (1.5×10^{-3} mol methane per 1 mol water at 5 MPa and 25 °C (Lide and Frederikse 1995)). This low solubility necessitates extensive pore fluid circulation and long experimental time for hydrate formation from the aqueous phase (Spangenberg *et al.* 2005).

We used THF, which forms hydrates at atmospheric pressure and temperature of 4 °C (Sloan and Koh 2008). THF is a heterocyclic ether with the molecular formula C_4H_8O. THF is completely miscible in water (Sloan and Koh 2008) and thus is widely used to resemble hydrate formation from methane dissolved in water (Pearson, Murphy, and Hermes 1986; Collett and Ladd 2000; Yun *et al.* 2005). Lee *et al.* (2007) demonstrated that THF and methane hydrates exhibit similar macro-scale mechanical, electrical, and thermal characteristics. THF has the advantage of providing close control on the hydrate saturation by varying the stoichiometric THF–H_2O mixture without having the long formation history of methane hydrates. However, it should be noted that THF hydrate forms structure II hydrates, whereas pure methane forms structure I hydrates. Hydrates in nature, particularly when formed from thermogenic gas, often contain longer chain hydrocarbons (e.g., ethane and propane) in addition to methane and thus can form structure II hydrates (Sloan and Koh 2008). Further, the velocity difference for structure I and II hydrates is small compared with the variation in velocities caused by different pore-space hydrate distributions (Sloan and Koh 2008). The velocity difference caused by using a structure II instead of a structure I hydrate is negligible. Therefore, the THF hydrate is used as a proxy for naturally occurring gas hydrates. Since THF is completely miscible in water, there is no interface between the two phases. Thus, THF does resemble the hydrate formation from methane dissolved in water and not the formation from free gas and water.

Sample composition and preparation

Sample components were unconsolidated borosilicate glass beads (diameter: 1 mm) used as the host sediment, deionised water, THF, and barium chloride. In contrast to sediment grains, glass beads have a uniform X-ray attenuation value, shape, and density (2.23 g/cm^3), allowing for easier interpretation of the micro CT images. We used barium chloride as a CT contrast agent and a proxy for naturally occurring sodium chloride brine. Stoichiometric mixtures of THF and water were used to obtain different hydrate saturations. The

Table 1 List of measured samples

S_h	Ultrasonic	Micro CT
40%	2	1
60%	0	2
80%	2	1
100%	0	1

specimen exhibited porosity of approximately 0.35. The porosity was determined from CT images.

The same sample composition was used for ultrasonic velocity measurements and micro CT imaging. For the micro CT samples, the liquid mixture of THF, barium chloride, and deionised water was added to the dry borosilicate glass beads through a syringe. Micro CT samples were formed directly in the pressure vessel and had a pore volume of approximately 3 ml. For the ultrasonic samples, a sleeve of heat-shrink tubing was placed between two ultrasonic transducers, filled with borosilicate glass beads and then evacuated before the mixture of THF, water, and barium chloride was injected with a pore pressure of 0.3 MPa. The glass beads were poured into a heat-shrink sleeve loosely without compacting them. The pore volume of the ultrasonic samples was 9.4 ml.

Table 1 shows all samples that have been measured. Micro CT imaging was performed on four samples: two with 40% hydrate saturation and two with 80% hydrate saturation. Ultrasonic velocity measurements were obtained for five samples with saturations of 40%, 60%, 80%, and 100%, and one additional sample with 60% hydrate saturation that did not contain barium chloride. These saturations were chosen to compare the measured ultrasonic velocities with the effective medium models. Note that the reported THF hydrate saturations refer to the target hydrate saturation that we expect from the water–THF ratio for each sample. Due to THF evaporation and incomplete conversion of THF and water to hydrate, the actual saturation of our samples will probably be below the target saturation.

Micro X-ray computed tomography

Micro CT imaging was performed in the MicroXCT-400 apparatus from XRadia. A Torlon (polyamide-imide) pressure cell with stainless-steel fittings on both ends was used. The pressure cell has an inner diameter of 7 mm and a length of 8 cm (Fig. 2). The setup was temperature controlled by cooled air. Air from a compressor is transported through a copper-coil located in a cooling bath ($T_{bath} = -30$ °C) and then led

through a thermally insulated hose into the CT apparatus. The insulated section between the cooling bath and CT apparatus also contains a hose loop that circulates cooled ethylene glycole alongside the air hose for additional cooling. This setup provides cooling for periods of multiple days to keep the hydrate stable while high-resolution CT scans are performed. The temperatures were kept stable 1±0.5 °C for the duration of the imaging process. The temperature was constantly kept above 0 °C to avoid the formation of ice along with the THF hydrates. Temperature was measured with a thermocouple located directly in the glass bead pack.

Micro CT measurements allow the distinction between materials based on their X-ray attenuation. X-ray attenuation is proportional to a product of bulk density and effective atomic number of each material at the measurement X-ray energy (Van Geet, Swennen, and Wevers 2000). Thus, micro CT imaging provides insight into the distribution of different sample components in the pore space. The output data of the micro CT apparatus are greyscale images scaled to the X-ray attenuation. Dark grey areas indicate low attenuation, whereas light grey to white areas correspond to high attenuation.

Barium chloride was added to the fluid mixture to enhance the density contrast between the residual brine and hydrate. A higher density contrast leads to a contrast in X-ray attenuation and thus to distinguishable grey values in the images. As hydrates form, barium chloride is excluded from the hydrate structure and remains within the water phase. The bulk densities of each sample component are listed in Table 2. We used an initial salinity level of 3.2% for the sample with 80% hydrate saturation and 8.3% for the sample with 40%, resulting in a salinity level of 12.3% in the residual brine for both samples after hydrate formation. The amount of barium chloride was adjusted for each sample in order to obtain a density of 1.1 g/cm^3 for the remaining water, assuming that all THF in the sample has been converted to hydrates.

In this study, the hydrate-bearing sample was monitored after the hydrate formation process was completed. Micro CT imaging of THF-hydrate dissociation was discussed by Schindler and Batzle (2014). X-ray source voltage of 150 kV and power of 6.2 W were used for all tomography scans. Magnification of 0.5× (resolution: 14.9 and 45.4 μm) was used to obtain a large field of view and thus an overview over the sample, and magnification of 4× (resolution: 5 μm) was used for a detailed view of the pore space. Best results were obtained for angular increments of 0.1° to 0.2°, resulting in scanning duration of 1.5 h for 0.5× magnification to 6 h for 4× magnification.
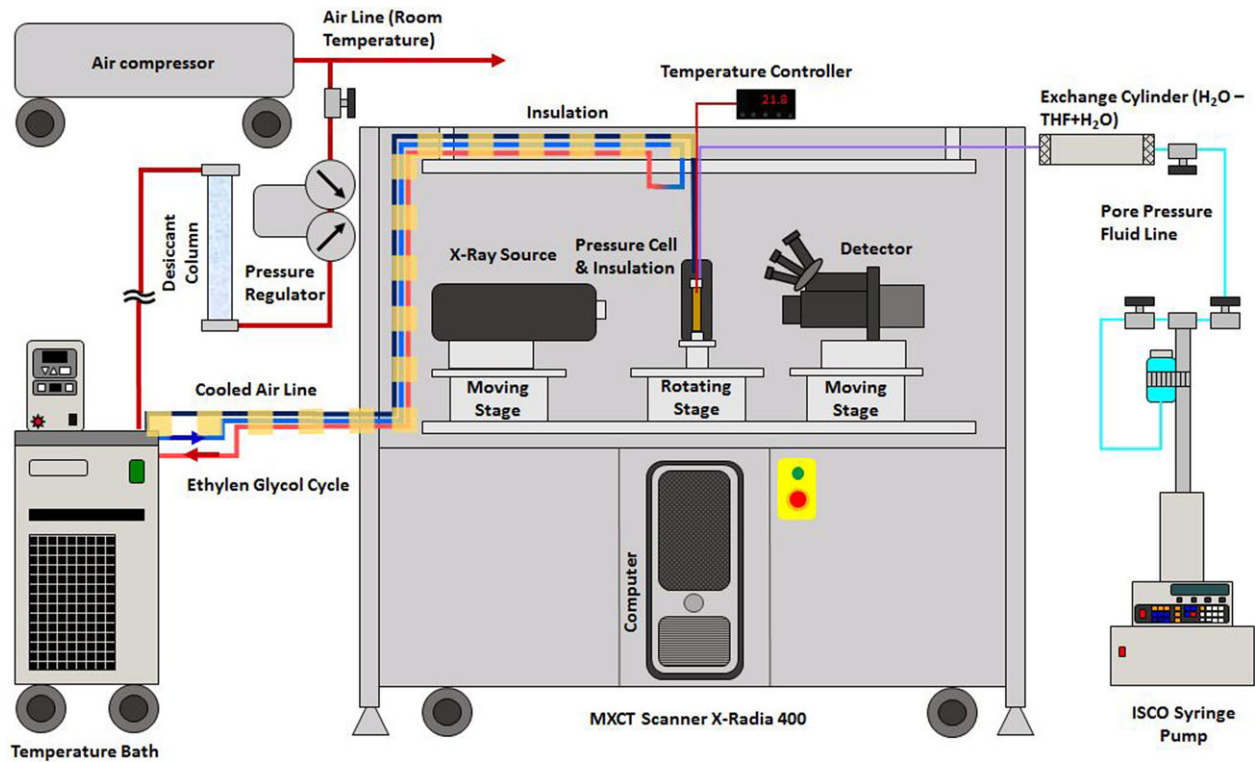
Figure 2 Experimental setup for micro CT imaging.

Ultrasonic velocity measurements

The basic principle behind pulse-transmission ultrasonic velocity measurements is to send an ultrasonic signal through a sample and measure the signal's travel time. Therefore, transducers with piezoelectric PZT crystals (frequency: 500 kHz) for P-waves and S-waves are attached to a sample jacketed with heat-shrink tubing. Temperatures are recorded with a thermocouple located outside of the sample in the confining fluid. Figure 3 shows a schematic of the experimental setup. More detailed information about the experimental setup and methodology can be found in Schindler and Batzle (2014).

Table 2 Density of sample components included in micro CT samples. (a) From Lide and Frederikse (1995). (b) from Sloan and Koh (2008)

Component	Density [g/cm^3]
water	1.00
BaCl$_2$	3.84[a]
BaCl$_2$ brine (12.3 wt%)	1.1
THF hydrate	0.97[b]
THF-water-BaCl$_2$ mixture	1.00

After the described sample preparation, an isostatic confining pressure of 3.3 MPa was applied, and the temperature was gradually decreased below hydrate stability temperature (4.3 °C for 100% THF hydrate saturation). Waveforms for compressional and shear waves were recorded during the cooling process for each 1 °C interval. At temperatures close to the hydrate stability zone, waveforms were recorded more frequently (approximately every 0.2 °C). The cooling process was continued until hydrate formed in the sample which was indicated by a significant increase in compressional and shear wave velocities. When a significant increase in velocities was observed, the temperature was kept constant until the velocities stabilised. After hydrate formation, the sample was cooled further until the remaining water in the pore space froze. The ice formation was indicated by an additional increase in velocities at lower temperatures than the first velocity increase. The further cooling until ice formation was performed to rule out ice as the reason for the first observed velocity increase. Differential scanning calorimetry has shown that the addition of 5 wt% barium chloride decreases the freezing temperature of ice to −7.9 °C and the hydrate equilibrium temperature to 3.8 °C. Thus, the samples had to be cooled below 0 ° to form ice.
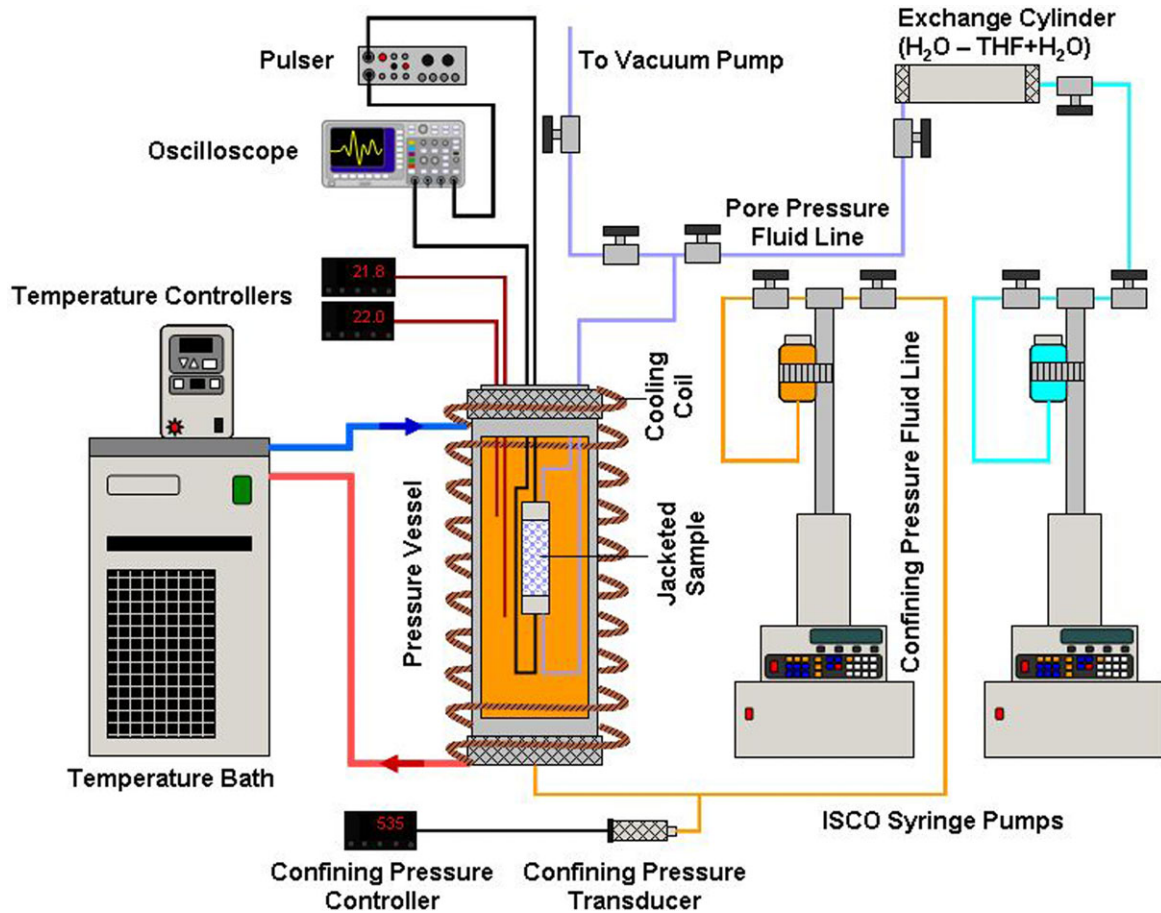
Figure 3 Experimental setup for ultrasonic velocity measurements.

First arrival times were picked from waveforms (Fig. 4). The sample length was determined from micro CT imaging of the sample before performing the ultrasonic velocity measurements and a second time after performing the measurements for comparison. Ultrasonic velocities can be determined from arrival time and sample length:

$$v = \frac{l}{t - t_0}, \tag{1}$$

where l is the length of the sample, t is the first arrival time, and t_0 is the dead time (the total travel time of a pulse when one transducer assembly is in contact with the other without a sample in between).

RESULTS AND DISCUSSION

Micro X-ray computed tomography imaging

The reconstructed computed tomography (CT) images (Fig. 5) contain information about the distribution of different components in the samples. Different grey values in the CT images represent different X-ray attenuation values in the sample. Because of its low attenuation (Table 2), THF hydrate has low grey values and appears as violet and black areas in the micro CT images, whereas barium chloride brine has higher grey values caused by its higher attenuation value (Table 2) and is displayed in light yellow and white.

Figure 5 shows CT images for two samples with 40% and 80% hydrate saturation. The images indicate that the THF hydrate is located in the pore body. However, part of the hydrate appears to bridge the grains and becomes load bearing. Barium chloride brine is found mainly at the grain contacts and fills some small pores entirely. These observations are in agreement with the findings by Kerkar *et al.* (2014) and Chaouachi *et al.* (2015). Both observed a layer of residual water between the hydrate and grain surface, indicating no cementation of the grains by the hydrate. Due to resolution limitations, the residual water layer was not observed in our micro CT images. The hydrate can have load bearing behaviour
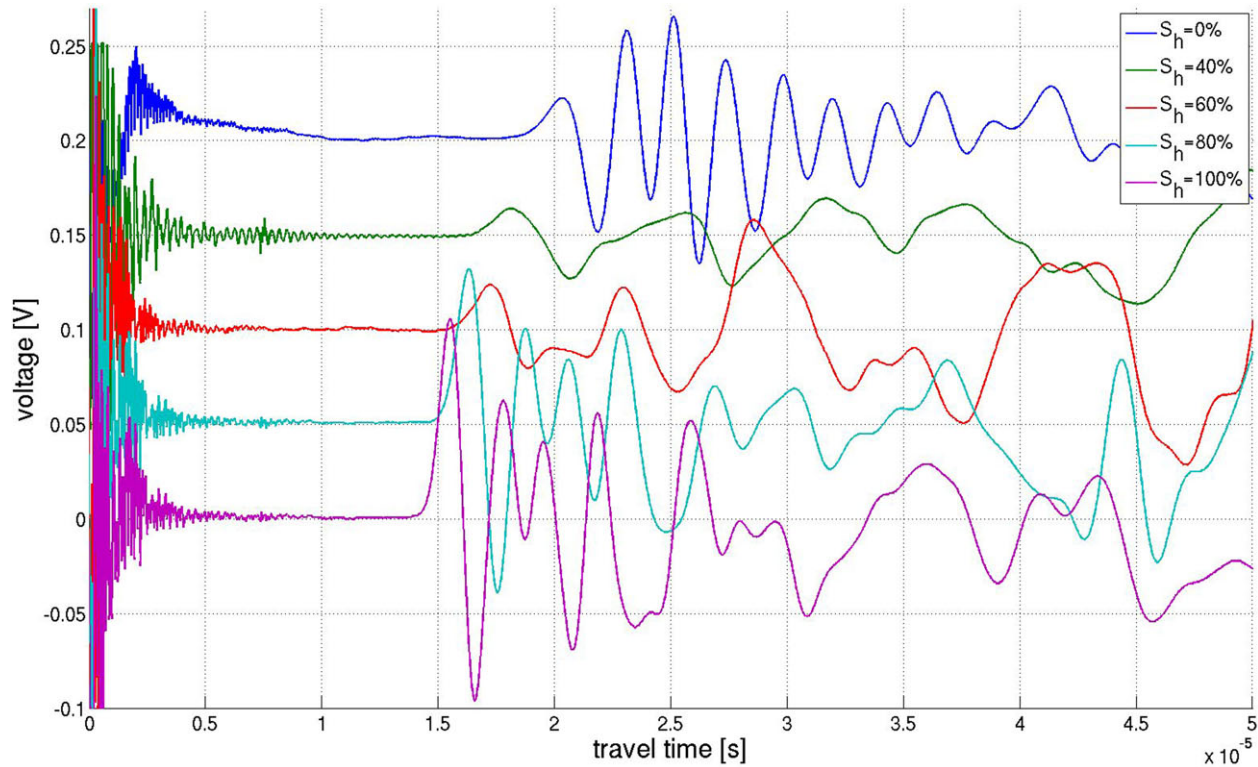
Figure 4 Ultrasonic waveforms of samples with different hydrate saturations. A decrease in P-wave arrival times with increasing hydrate saturation was observed.
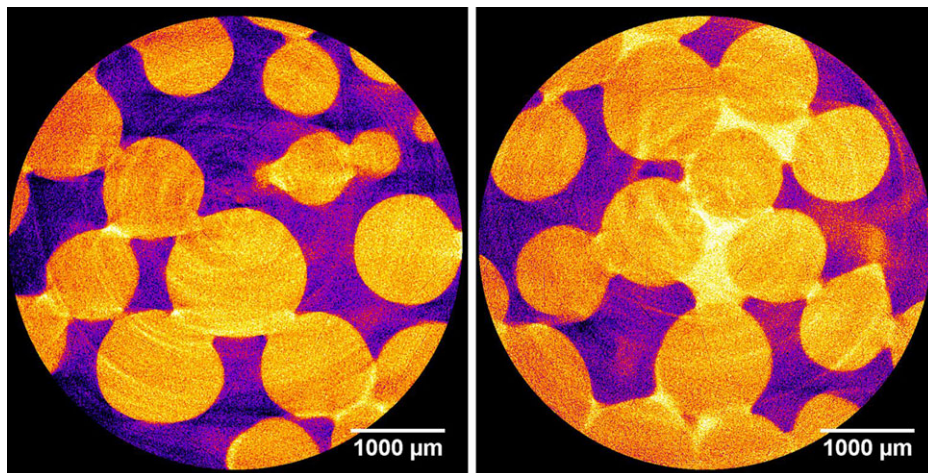

Figure 5 CT image showing horizontal slice through sample with (left) $S_h = 40\%$ and (right) $S_h = 80\%$. Resolution of 5.0 μm. White/light yellow: Barium chloride brine. Yellow/orange: Glass beads. Pink/violet: THF hydrate.

even in the presence of a residual water layer between hydrate and sediment grains. The presence of hydrate in the pore space restricts the movement of sediment grains and thus increases moduli and velocities, respectively, without hydrate crystals directly touching the grain surfaces. THF hydrate is distributed evenly throughout the entire sample; heterogeneity was not observed. For image analysis, *ImageJ* was used.[1]

---

[1] ImageJ is a free image processing package mainly used for medical imaging. It is available at http://imagej.nih.gov/ij/

Table 3 Ultrasonic velocities after hydrate formation

S_h [%]	v_p [m/s]	v_s [m/s]
0	2078 ± 83	658 ± 131
40 ± 5	2512 ± 123	1025 ± 218
60 ± 5	2645 ± 133	1057 ± 233
80 ± 5	3021 ± 146	1185 ± 255
100 ± 5	3466 ± 189	1187 ± 275

Ultrasonic velocity measurements

P-wave and S-wave velocities were recorded for each sample during the cooling from 23 °C to −8 °C; they are shown exemplary for the sample with 40% hydrate saturation in Fig. 7. The errors for P and S-wave velocities are about 5% and 20% to 23%, respectively (Table 3). Errors in velocity were calculated by propagating the uncertainties in sample length and picking of arrival times:

$$\sigma_v = v \sqrt{\sigma_l^2 \left(\frac{\partial v}{\partial l}\right)^2 + \sigma_t^2 \left(\frac{\partial v}{\partial t}\right)^2 + \sigma_{t_0}^2 \left(\frac{\partial v}{\partial t_0}\right)^2}, \qquad (2)$$

where v is the velocity, l is the length of the sample, t is the arrival time, t_0 is the dead time, σ_l is the uncertainty in sample length, σ_t is the uncertainty in arrival time, σ_{t_0} is the uncertainty in dead time, and σ_v is the absolute error in velocity.

The sample length was determined with micro CT in four different positions. Half of the difference between the longest and the shortest measured lengths was used as the error in sample length. This length uncertainty was between 200 and 400 μm for all measured samples. It should be noted that the variation in length due to applied confining pressure and hydrate formation in the sample can be larger - thus introducing an additional but not quantifiable error. The arrival time for the compressional wave is picked manually at the first significant divergence from zero in amplitude. Since the manual pick is subjective, an error of $\sigma_t = 10^{-7}$s is assumed. The shear wave is picked at the first amplitude maximum since the first divergence from zero for the shear wave is not visible due to signal quality. This introduces an error of $\sigma_t = 5 \cdot 10^{-6}$s, resulting in a much larger velocity error for the S-wave than for the P-wave. However, the arrival times were picked at the same feature for each of the waveforms. Thus, the relative
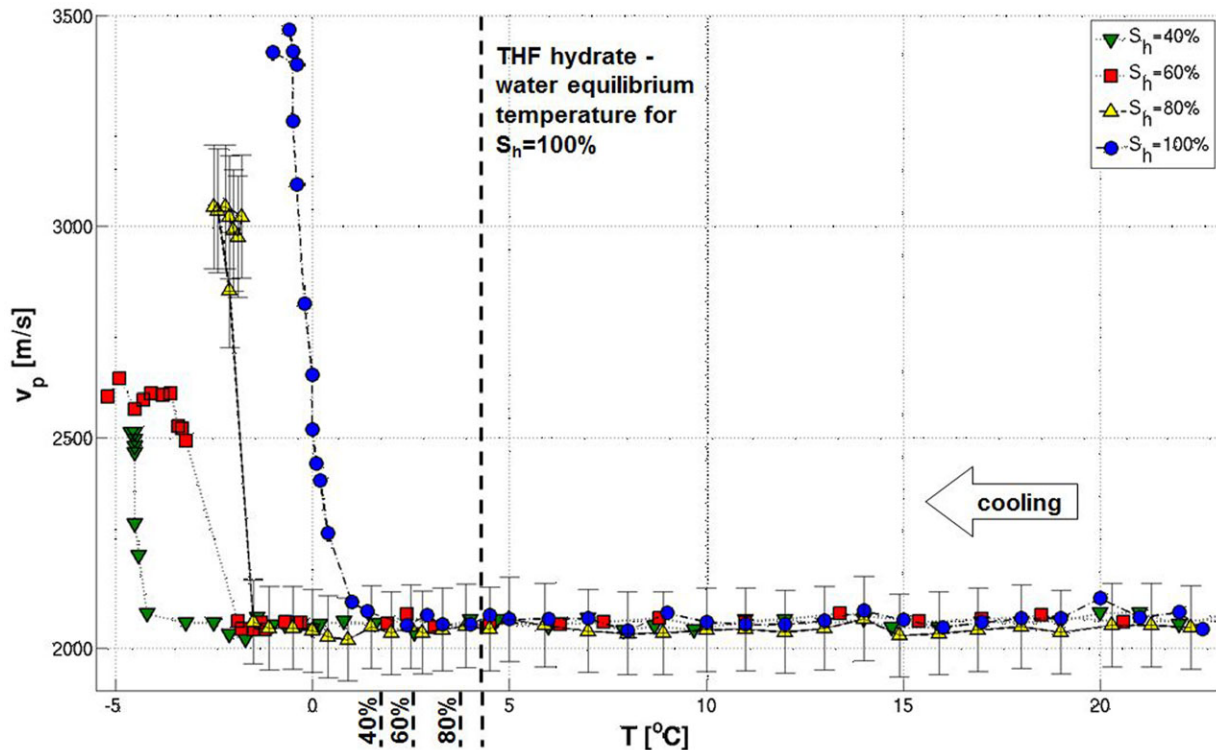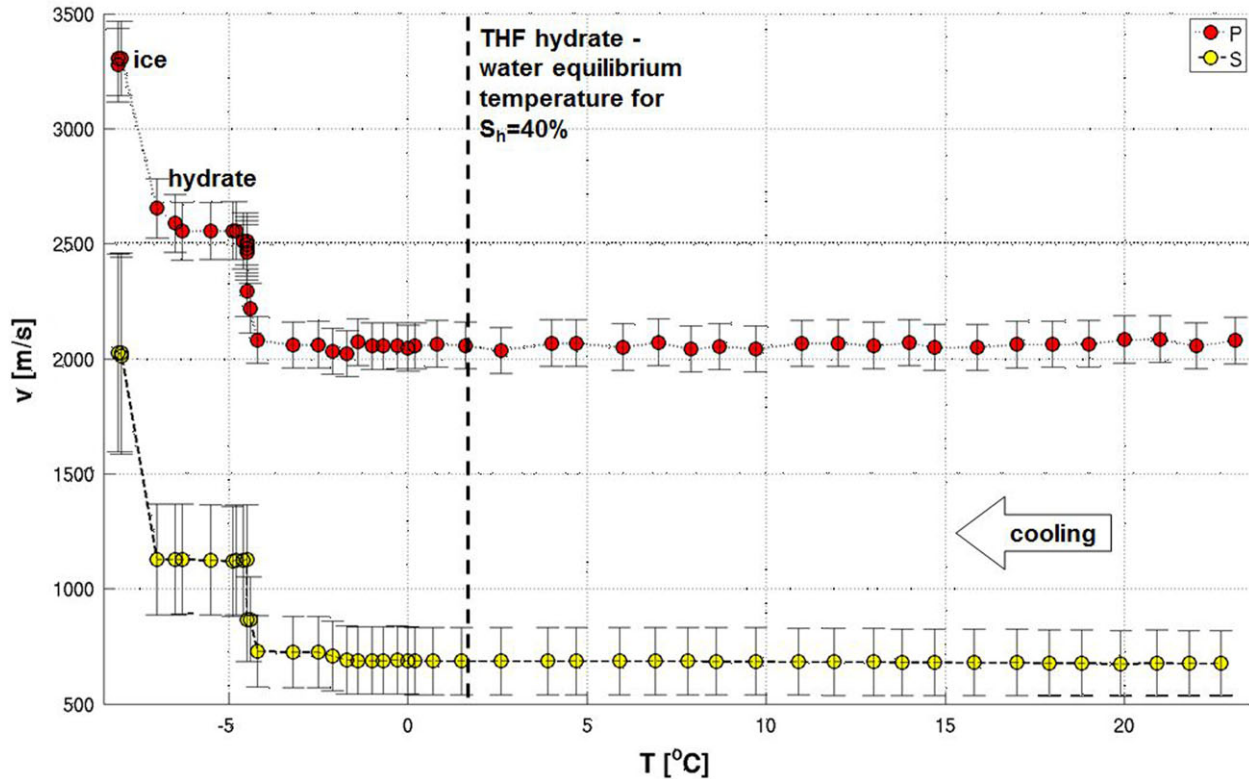

Figure 6 Ultrasonic P-wave velocities during the cooling of samples with different hydrate saturations. The THF-hydrate–water equilibrium temperature is shown for each tested hydrate saturation. An increase in velocities indicates the presence of hydrate in the sample. Higher hydrate saturation resulted in higher P-wave velocities. For illustration, velocity error bars are shown for 80% hydrate saturation. The formation of ice was decreased to about -8 °C due to the addition of barium chloride.

Figure 7 Ultrasonic P-wave and S-wave velocities recorded during the cooling of a sample with 40% hydrate saturation. The THF-hydrate–water equilibrium boundary is shown for 40% hydrate saturation. After hydrate formation, the sample was cooled further until the residual water froze, resulting in an additional velocity increase.

error is much smaller than the absolute error displayed in Fig. 7 and Table 3. Our analysis concentrates on P-wave velocities because of the large error in S-wave velocities. An error of 5% is assumed for hydrate saturations. The vapour pressure of THF is six to seven times higher than that of water. Thus, THF will evaporate preferentially, causing the actual hydrate saturation to be lower but never higher than the target saturation (Yun, Santamarina, and Ruppel 2007). Thus, we show error bars for the hydrate saturations only in a negative direction. Yun *et al.* (2007) assumed 2% of THF hydrate saturation uncertainty for their study.

The equilibrium temperature for THF hydrates and water is 4.3 °C for 100% hydrate saturation. Hydrate formation started at temperatures below 4.3 °C. Reasons are the addition of barium chloride and the sub-cooling required to initiate hydrate formation (Sloan and Koh 2008). Furthermore, 4.3 °C is the equilibrium temperature for 100% hydrate saturation. For lower hydrate saturations, the equilibrium temperature decreases (Sloan and Koh 2008), as shown in Fig. 6. Additionally, the temperature was recorded in the confining fluid outside of the sample, and the system was cooled radially

from the outside inward. Thus, it is assumed that the temperature of the sample was slightly higher than the measured temperatures during the cooling process. An increase in velocities, which is attributed to the presence of hydrate in the pore space, was first observed below 0 °C for all samples except for 100% hydrate saturation. A second velocity increase indicated the formation of ice at lower temperatures of approximately −8 °C (Fig. 7). Although the hydrate formation started at temperatures below 0 °C, the simultaneous formation of ice in the sample can be ruled out due to the second increase in velocities.

Figure 6 shows the P-wave velocities recorded during the cooling of four samples with four different hydrate saturations. The velocities remain approximately constant before THF hydrate stability temperature is reached. A velocity increase became apparent at temperatures below the THF hydrate stability temperature, which decreases with decreasing hydrate saturation (Makino, Sugahara, and Ohgaki 2005). The velocity increases with hydrate saturation increase. We speculate that the hydrate formation starts before we observe an increase in P- and S-wave velocities. The THF hydrate
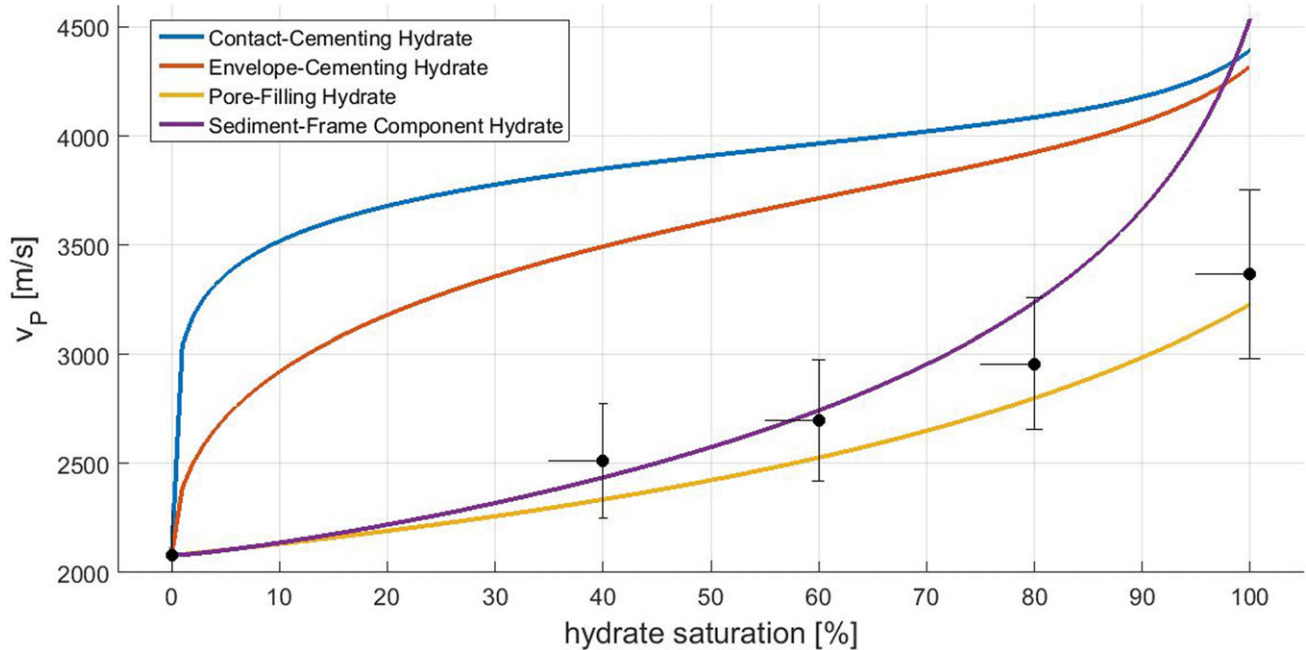
Figure 8 Effective medium model after Ecker *et al.* (1998) and Helgerud *et al.* (1999) with compressional wave velocities obtained by ultrasonic measurements.

forms first in small amounts in the pore fluid and is not detected by the ultrasonic velocities. As the hydrate saturation increases and hydrate starts to bridge the grains, we see significant increases in velocities (Figs. 6 and 7). Similar observations were made by (Hu *et al.* 2010) who reported changes in P-wave and S-wave velocities only when hydrate saturation exceeds 10%.

Figure 8 demonstrates how the measured ultrasonic velocities at different THF hydrate saturations compare with the effective medium models by Ecker *et al.* (1998) and Helgerud *et al.* (1999). The input parameters for the effective medium models are listed in Tables 4 and 5. P-wave velocities follow the trend of the pore-filling model but show higher values. We attribute these higher values to the partial bridging of grains

Table 4 Input parameters for effective medium models (hydrate data from Sloan and Koh (2008) and brine and THF data from Lide and Frederikse (1995))

Component	ρ [kg/m^3]	K [GPa]	G [GPa]
glass beads	2230	34.6	26.2
brine (12.3 wt%)	1100	2.3	0
THF	889	2.1	0
THF hydrate	970	8.7	3.6

Table 5 Input parameters for effective medium models (hydrate data from Sloan and Koh (2008) and brine and THF data from Lide and Frederikse (1995))

coordination number	9
porosity	0.35
critical porosity	0.36
effective pressure	3 MPa

that causes the THF hydrate to have a load-bearing behaviour. The effective medium models show end members of possible hydrate distributions. A mixing of the hydrate suspended in the pore fluid with the hydrate partially bridging grains and becoming part of the sediment frame is possible. This behaviour has been described by Fabricius (2003) as isoframe models. The observation of non-cementing hydrate that is mainly located in the pore bodies is in agreement with findings in natural hydrate samples from the Nankai Trough (Inamori *et al.* 2010; Konno *et al.* 2015; Santamarina *et al.* 2015).

CONCLUSION

The micro X-ray computed tomography (CT) images showed that the THF hydrate forms in the pores as part of the pore

fluid, but at high hydrate saturations, we observed a partial bridging of the grains by load-bearing hydrates. Ultrasonic velocities increase only after cooling the sample well below the THF hydrate stability temperature. We conclude that THF hydrate first forms in the pore bodies. Ultrasonic velocities increase only after hydrate saturation increases enough for the hydrate to become load bearing. Direct contact between hydrate crystals and sediment grains is not necessary for the hydrate to be load bearing. Although we did not observe a residual water layer separating hydrate and sediment grains, previous studies indicated the presence of such a layer and no direct contact between hydrate and grain surfaces. Given that THF hydrate is a proxy for one possible texture of natural occurring hydrate, we conclude that natural gas hydrates in coarse-grained sediments are partially suspended in the pore fluid and are partially load bearing when formed from natural gas dissolved in water. This conclusion is essential for the assessment of gas hydrate saturation from seismic and sonic log data. The combination of micro CT imaging and ultrasonic velocity measurements in our study allows a direct visible observation of the hydrate distribution in the pore space linked to the effect of said hydrate distribution on elastic properties. Our study provides a verification of pore-scale hydrate distribution, which is indirectly implied from elastic properties in other publications.

ACKNOWLEDGMENTS

REFERENCES

Anderson B.J., Wilder J.W., Kurihara M., White M.D., Moridis G.J., Wilson S.J. *et al.* 2008. Analysis of modular dynamic formation test results from the Mount Elbert 01 stratigraphic test well, Milne Point Unit, North Slope, Alaska. In: *Proceedings of the 6th International Conference on Gas Hydrates*.

Boswell R. and Collett T.S. 2006. Fire in the ice: the gas hydrates resource pyramid. *NETL Newsletter*, 5–7.

Chand S., Minshull T.A., Priest J.A., Best A.I., Clayton C.R.I. and Waite W.F. 2006. An effective medium inversion algorithm for gas hydrate quantification and its application to laboratory and borehole measurements of gas hydrate-bearing sediments. *Geophysical Journal International* **166**(2), 543–552.

Chaouachi M., Falenty A., Sell K., Enzmann F., Kersten M., Haberthür D. *et al.* 2015. Microstructural evolution of gas hydrates in sedimentary matrices observed with synchrotron X-ray computed tomographic microscopy. *Geochemistry, Geophysics, Geosystems* **16**(6), 1711–1722.

Collett T.S., Johnson A.H., Knapp C.C. and Boswell R. 2009. Natural gas hydrates: a review. In: *Natural Gas Hydrates –Energy Resource Potential and Associated Geologic Hazards: AAPG Memoir 89*, pp. 146–219.

Collett T.S. and Ladd J. 2000. Detection of gas hydrate with downhole logs and assessment of gas hydrate concentrations (saturations) and gas volumes on the Blake Ridge with electrical resistivity log data. In: *Proceedings of the Ocean Drilling Program. Scientific Results Vol. 164*, pp. 179–191. Ocean Drilling Program.

Collett T.S. and Lee M.W. 2012. Well log characterization of natural gas-hydrates. *Petrophysics* **53**(5), 348–367.

Dallimore S.R., Wright J.F., Nixon F.M., Kurihara M., Yamamoto K., Fuji K. *et al.* 2008. Geologic and porous media factors affecting the 2007 production response characteristics of the JOGMEC/NRCAN/AURORA Mallik gas hydrate production research well. In: *Proceedings of the 6th International Conference on Gas Hydrates*.

Dobrynin V.M., Korotajev Yu.P. and Plyuschev D.V. 1981. Gas hydrates –a possible energy resource. In: *Long-Term Energy Resources* (eds. R.F. Meyer and J.C. Olson), pp. 727–729. Pitman Publishing, Boston, MA, USA.

Dvorkin J. and Nur A. 1996. Elasticity of high-porosity sandstones: theory for two North Sea data sets. *Geophysics* **61**(5), 1363–1370.

Dvorkin J., Nur A. and Yin H. 1994. Effective properties of cemented granular materials. *Mechanics of Materials* **18**(4), 351–366.

Ebinuma T., Kamata Y., Minagawa H., Ohmura R., Nagao J. and Narita H. 2005. Mechanical properties of sandy sediment containing methane hydrate. In: *Proceedings of Fifth International Conference on Gas Hydrates*, Vol. 3037, pp. 958–961.

Ecker C., Dvorkin J. and Nur A. 1998. Sediments with gas hydrates: internal structure from seismic AVO. *Geophysics* **63**(5), 1659–1669.

Fabricius I.L. 2003. How burial diagenesis of chalk sediments controls sonic velocity and porosity. *AAPG Bulletin* **87**(11), 1755–1778.

Helgerud M.B., Dvorkin J., Nur A., Sakai A. and Collett T.S. 1999. Elastic-wave velocity in marine sediments with gas hydrates: Effective medium modeling. *Geophysical Research Letters* **26**(13), 2021–2024.

Hu G.W., Ye Y.G., Zhang J., Liu C.L., Diao S.B. and Wang J.S. 2010. Acoustic properties of gas hydrate-bearing consolidated sediments and experimental testing of elastic velocity models. *Journal of Geophysical Research: Solid Earth* **115**(B2).

Inamori T., Hato M., Suzuki K. and Saeki T. 2010. The rock physics model in the unconsolidated methane hydrate bearing sediments. *Journal of the Japanese Association for Petroleum Technology* **75**(1), 59–71.

Kerkar P.B., Horvat K., Jones K.W. and Mahajan D. 2014. Imaging methane hydrates growth dynamics in porous media using synchrotron X-ray computed microtomography. *Geochemistry, Geophysics, Geosystems* **15**(12), 4759–4768.

Kerkar P.B., Jones K.W., Kleinberg R., Lindquist W.B., Tomov S., Feng H. *et al.* 2009. Direct observations of three dimensional growth of hydrates hosted in porous media. *Applied Physics Letters* **95**(2), 024102.

Konno Y., Jin Y., Yoneda J., Kida M., Egawa K., Ito T. *et al.* 2015. Effect of methane hydrate morphology on compressional wave velocity of sandy sediments: analysis of pressure cores obtained in the Eastern Nankai Trough. *Marine and Petroleum Geology* **66**, 425–433.

Kunerth D.C., Weinberg D.M., Rector J.W., Scott C.L. and Johnson J.T. 2001. Acoustic laboratory measurements during the formation of a THF-hydrate in unconsolidated porous media. *Journal of seismic exploration* **9**(4), 337–354.

Lee J.Y., Yun T.S., Santamarina J.C. and Ruppel C. 2007. Observations related to tetrahydrofuran and methane hydrates for laboratory studies of hydrate-bearing sediments. *Geochemistry, Geophysics, Geosystems* **8**(6).

Lide D.R. and Frederikse H.P.R. 1995. *CRC Handbook of Chemistry and Physics*. CRC Press.

Makino T., Sugahara T. and Ohgaki K. 2005. Stability boundaries of tetrahydrofuran+ water system. *Journal of Chemical & Engineering Data* **50**(6), 2058–2060.

Meyer R.F. 1981. Speculations on oil and gas resources in small fields and unconventional deposits. *Long-term Energy Resources* **1**, 49–72.

Pearson C., Murphy J. and Hermes R. 1986. Acoustic and resistivity measurements on rock samples containing tetrahydrofuran hydrates: laboratory analogues to natural gas hydrate deposits. *Journal of Geophysical Research: Solid Earth* **91**(B14), 14132–14138.

Priest J.A., Best A.I. and Clayton C.R.I. 2005. A laboratory investigation into the seismic velocities of methane gas hydrate-bearing sand. *Journal of Geophysical Research: Solid Earth* **110**(B4).

Rydzy M.B. and Batzle M.L. 2011. Rock physics characterization of THF hydrate bearing sediment. In: *Proceedings of the 7th International Conference on Gas Hydrates*.

Santamarina J.C., Dai S., Terzariol M., Jang J., Waite W. F., Winters W.J. *et al.* 2015. Hydro-bio-geomechanical properties of hydrate-bearing sediments from Nankai Trough. *Marine and Petroleum Geology* **66**, 434–450.

Schindler M. and Batzle M.L. 2014. Pore-scale investigation of hydrate-bearing sediments. In: *Pore Scale Phenomena: Frontiers in Energy and Environment* (eds J.M. Poate, H. Kazemi, T.H. Illangasekare, and R.J. Kee). World Scientific, Golden, CO, USA.

Sloan E.D. and Koh C.A. 2008. *Clathrate Hydrates of Natural Gases*. CRC Press.

Sothcott J., Ellis M.H., Best A.I., Frerichs N.R., Minshull T.A. and Sinha M.C. 2007. Laboratory observations of morphology, velocity, attenuation and resistivity of methane gas hydrate bearing rocks. 77th SEG meeting, San Antonio, USA, Expanded Abstracts, 1530–1533.

Spangenberg E., Kulenkampff J., Naumann R. and Erzinger J. 2005. Pore space hydrate formation in a glass bead sample from methane dissolved in water. *Geophysical Research Letters* **32**(24).

Van Geet M., Swennen R. and Wevers M. 2000. Quantitative analysis of reservoir rocks by microfocus X-ray computerised tomography. *Sedimentary Geology* **132**(1–2), 25–36.

Waite W.F., Winters W.J. and Mason D.H. 2004. Methane hydrate formation in partially water-saturated Ottawa sand. *American Mineralogist* **89**(8–9), 1202–1207.

Waite W.F., Santamarina J.C., Cortes D.D., Dugan B., Espinoza D.N., Germaine J. *et al.* 2009. Physical properties of hydrate-bearing sediments. *Reviews of Geophysics* **47**(4).

Yun T.S., Francisca F.M., Santamarina J.C. and Ruppel C. 2005. Compressional and shear wave velocities in uncemented sediment containing gas hydrate. *Geophysical Research Letters* **32**(10).

Yun T.S., Santamarina J.C. and Ruppel C. 2007. Mechanical properties of sand, silt, and clay containing tetrahydrofuran hydrate. *Journal of Geophysical Research: Solid Earth* **112**(B4).